

Role of charge transfer, dipole-dipole interactions, and electrostatics in Fermi-level pinning at a molecular heterojunction on a metal surface

P. Amsalem,^{1,*} J. Niederhausen,¹ A. Wilke,¹ G. Heimel,¹ R. Schlesinger,¹ S. Winkler,^{1,2} A. Vollmer,² J. P. Rabe,¹ and N. Koch^{1,2}

¹Humboldt-Universität zu Berlin, Institut für Physik, Newtonstr. 15, 12489 Berlin, Germany

²Helmholtz-Zentrum Berlin für Materialien und Energie GmbH, BESSY II, Albert-Einstein-Str. 15, 12489 Berlin, Germany

(Received 21 November 2012; published 31 January 2013)

Recently, Niederhausen *et al.* [*Phys. Rev. B* **86**, 081411(R) (2012)] have reported on the energy level alignment of C₆₀ adsorbed on a bilayer α -sexithiophene (6T) film on Ag(111). The possibility of charge transfer from the metal to the C₆₀ through the bilayer 6T as discussed by the authors may have a strong impact on understanding the energy level alignment (ELA) at organic-organic (O-O) heterojunctions grown on electrodes. In this paper, we aim at a comprehensive picture of the ELA at O-O interfaces on a metal. We carry out a detailed investigation of the same pair of materials on Ag(111) as employed previously, however, with varying 6T interlayer thickness. The results allow unambiguous identification of integer charge transfer towards a fraction of the C₆₀ molecules as the mechanism leading to the formation of interface dipoles. Varying the 6T interlayer thickness also reveals the dependence of the observed features on the C₆₀-metal distance. This dependence is quantitatively addressed by electrostatic considerations involving a metal-to-overlayer charge transfer. From this, we demonstrate the important role of dipole-dipole interaction potentials in the molecular layer and electric fields resulting from interface dipole formation for the energy level alignment. These findings provide a deeper understanding of the fundamental mechanisms that establish electronic equilibrium at molecular heterojunctions and will aid the prediction of an accurate energy level alignment at device relevant heterojunctions, e.g. in organic opto-electronic devices.

DOI: [10.1103/PhysRevB.87.035440](https://doi.org/10.1103/PhysRevB.87.035440)

PACS number(s): 79.60.Ht, 88.30.rf, 73.20.Hb, 81.05.ub

I. INTRODUCTION

During the past two decades, much effort has been devoted towards understanding and optimizing organic based (opto)electronic devices, such as light emitting diodes, solar cells, or field effect transistors. The efficiency of these devices depends strongly on the electronic properties of the interfaces between electrodes and organic materials, and also of organic heterojunctions, where energy barriers for charge transfer commonly exist.¹⁻⁶ In the case of organic-metal interfaces the validity of vacuum level (VL) alignment (Schottky-Mott limit) has been ruled out by the systematic observation of interface dipoles.^{5,7,8} The latter result from chemical bond formation, charge transfer, and molecular distortions, or more generally, are due to interfacial charge density rearrangements upon contact formation. Interface dipoles even occur when molecules are physisorbed on metals, and the charge density changes were identified to be due to Pauli repulsion.^{5,9,10} Over the years, calculations based on density functional theory (DFT) and beyond, such as van der Waals corrected DFT or hybrid methods including electron correlation effects, have been developed in order to capture the essential underlying physics of organic-metal interfaces.¹¹⁻¹⁹ Apart from DFT, other approaches have been proposed, consisting of (non-specific) phenomenological models to describe the electronic properties of these interfaces.²⁰⁻²² Despite the increasing modeling capabilities, no general rules have been established unequivocally yet to predict the energy level alignment, and it is still good advice today to address each specific interface experimentally.

For electrodes consisting of an organic layer on a metal, as well as for conductive polymers and contaminated electrodes, it was found experimentally that VL alignment holds for substrate work function (Φ) values in an interval between

the respective negative and positive pinning levels $\Phi^{\text{pin-}}$ and $\Phi^{\text{pin+}}$, which are specific for every organic semiconductor.²³⁻²⁵ The origin of the observed $\Phi^{\text{pin-}}$ and $\Phi^{\text{pin+}}$ values are still debated.^{22,23,25,26} Outside of this [$\Phi^{\text{pin-}}$, $\Phi^{\text{pin+}}$] interval, VL alignment would place the electrode Fermi level (E_F) in the occupied (unoccupied) density of states of the organic semiconductor, corresponding to an electronic nonequilibrium situation. In response, interface dipoles form such that E_F comes to lie within the energy gap of the semiconductor and equilibrium is reestablished; this phenomenon is commonly referred to as Fermi-level pinning (E_F pinning).^{23,24,27-29} The formation of interface dipoles suggests that charge transfer toward (or from) the molecular overlayer plays a considerable role in the E_F pinning mechanism. Several models have been proposed to explain the still controversially debated physics behind this phenomenon. These include (i) integer charge transfer across the interface and formation of polarons, (ii) partial charge transfer accompanied by induced mutual polarization, (iii) filling of tailing intragap states, (iv) induced density of interface states, and (v) electron-chemical-potential equilibration.^{22,23,26,30-32} All these theories agree on the involvement of charge transfer between overlayer and substrate as being instrumental for the interface dipole formation. In addition, when E_F pinning occurs, another particularly intriguing fact is that nonzero charge injection barriers (i.e. the energy difference between the respective frontier energy level and the Fermi level) have often been reported.^{23,26,33-36}

Recently, we reported on a system consisting of a metal single crystal precovered with an inert spacer layer [one monolayer of tris(8-hydroxyquinolinato)aluminum (Alq₃)] on top of which a strong electron organic acceptor [hexaazatriphenylene-hexacarbonitrile (HATCN)] was deposited.³⁷ This system was designed to start out of electronic equilibrium, and the lowest unoccupied molecular orbital (LUMO) level of

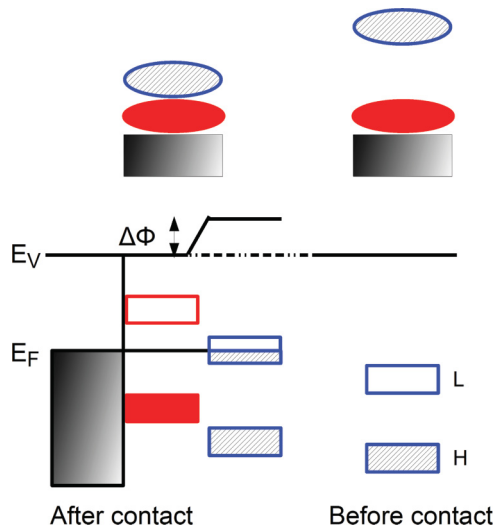


FIG. 1. (Color online) Schematic energy level diagram before and after contact of an electron acceptor organic overlayer (hatched) deposited on a metal precovered with an inert spacer layer (filled red). Electron transfer to the overlayer occurs upon contact and leads to the formation of an interface dipole $\Delta\Phi$. Filled/hatched and empty boxes depict the occupied and unoccupied states of the systems, respectively. H and L stand for HOMO and LUMO.

the acceptor overlayer was expected to become Fermi-level pinned, as depicted in Fig. 1. Because of the clear observation of interface density of states (DOS) upon adsorption, a metal-to-overlayer charge transfer (MOCT) was concluded on as the mechanism that establishes equilibrium via interface dipole formation. Related observations and conclusions were reported for depositing C_{60} on an α -sexithiophene (6T) bilayer precovered Ag(111).³⁸ In addition to an electron transfer from Ag(111) to C_{60} molecules, this system exhibited both charged and neutral C_{60} molecules within the C_{60} monolayer, which was suggested to be due to dipole-dipole repulsion. Furthermore, the role of concomitant electrostatic fields was considered for explaining the respective positions of the energy levels at this interface.

We now go beyond previous work to derive a more generally valid comprehensive picture of the energy levels for molecular heterojunctions in contact with a metal. Specifically, we investigate in detail the electronic properties of C_{60} deposited on one monolayer 6T (ML 6T) and a bilayer 6T (BL 6T) precovered Ag(111), whose structural properties were reported by Zhang *et al.* and Chen *et al.* previously.^{39,40} For both systems, we find an MOCT to a fraction of the C_{60} molecules within the overlayer. The proportion of charged and neutral molecules differs markedly for both systems, demonstrating a dependence on the overlayer-to-metal distance, i.e. the thickness of the 6T spacer layer. The potential drop observed in the spacer (6T) layer as well as the energy position of the neutral C_{60} frontier levels is proposed to result from electric fields induced by the interface dipoles. The above interpretation is further supported theoretically by classical electrostatics calculations. These findings allow establishing a coherent picture to explain the energy alignment at molecular (including organic-organic) interfaces in contact with metals, at least for thin films; however, it is foreseeable that, in the

future, this will turn out to also apply to cases of molecular and organic heterojunctions comprising thicker layers.

II. EXPERIMENTAL

The samples were prepared and analyzed *in situ* in ultra-high vacuum conditions. HeI and MgK α radiations were used for in-house ultraviolet photoelectron spectroscopy (UPS) and x-ray photoelectron spectroscopy measurements (XPS), respectively. Except for the clean Ag(111) spectrum, HeI- β and HeI- γ satellite lines (23.09 and 23.75 eV) were removed in the displayed spectra using standard procedures. High resolution XPS using synchrotron radiation was performed with a photon energy of 620 eV at the end station SurICat (beamline PM4) at the synchrotron light source BESSY II (Berlin, Germany). Photoemission spectra were collected in normal emission with a SPECS Phoibos 100 hemispherical energy analyzer (in-house) and with a hemispherical electron energy analyzer Scienta SES 100 (BESSY II) with 120 meV energy resolution. In all UPS and XPS spectra, the electron binding energies are referred to the sample Fermi level. Secondary electron cutoff (SECO, for determination of sample work function) was measured with -10 V bias applied to the sample. The Ag(111) surface was prepared by repeated Ar⁺ sputter-anneal (450 °C) cycles. C_{60} and 6T (Aldrich) were evaporated from resistively heated crucibles. The film thickness was monitored with a quartz microbalance using a density of 1.65 and 1.35 g.cm⁻³ for C_{60} and 6T, respectively. Under these conditions, one monolayer (ML) 6T is about 3 Å and 1 ML C_{60} is ~ 9 Å, as shown in the Results section. Details concerning the preparation of ML 6T and BL 6T can be found in Ref. 38.

III. RESULT AND DISCUSSION

A. C_{60} on ML 6T / Ag(111)

1. Valence band and core level spectra: Charged and neutral C_{60} within the first C_{60} monolayer

Figure 2 shows the valence electron region for C_{60} grown on ML 6T/Ag(111). Figures 2(a) and 2(b) show different energy ranges of a collection of valence band (VB) spectra corresponding, from bottom to top, to Ag(111), polycrystalline Ag [Fig. 2(a) only], ML 6T/Ag(111) (denoted 0*), and the subsequent C_{60} thickness-dependent series up to nominally 40 Å of C_{60} deposited on ML 6T/Ag(111). The most intense features in the bare Ag spectra between 4.0 and 7.5 eV binding energy (BE) correspond to the silver d band, and the flat background going from 4 eV BE up to E_F is due to the silver sp band. Upon formation of ML 6T on Ag(111), the Ag(111) d band changes dramatically and becomes very similar to the d band of polycrystalline Ag. This can be explained by Umklapp scattering (diffraction) of the substrate photoelectrons by the molecular overlayer.^{41–45} Additional intensity due to ML 6T is mostly visible between 1 and 4 eV BE.

In the zoom of the silver sp band region shown in Fig. 2(b), the intense and sharp peak located at E_F in the clean Ag(111) spectrum is due to the Ag(111) Shockley surface state. This state completely vanishes upon formation of ML 6T. This is possibly related to an upward energy shift of the Shockley

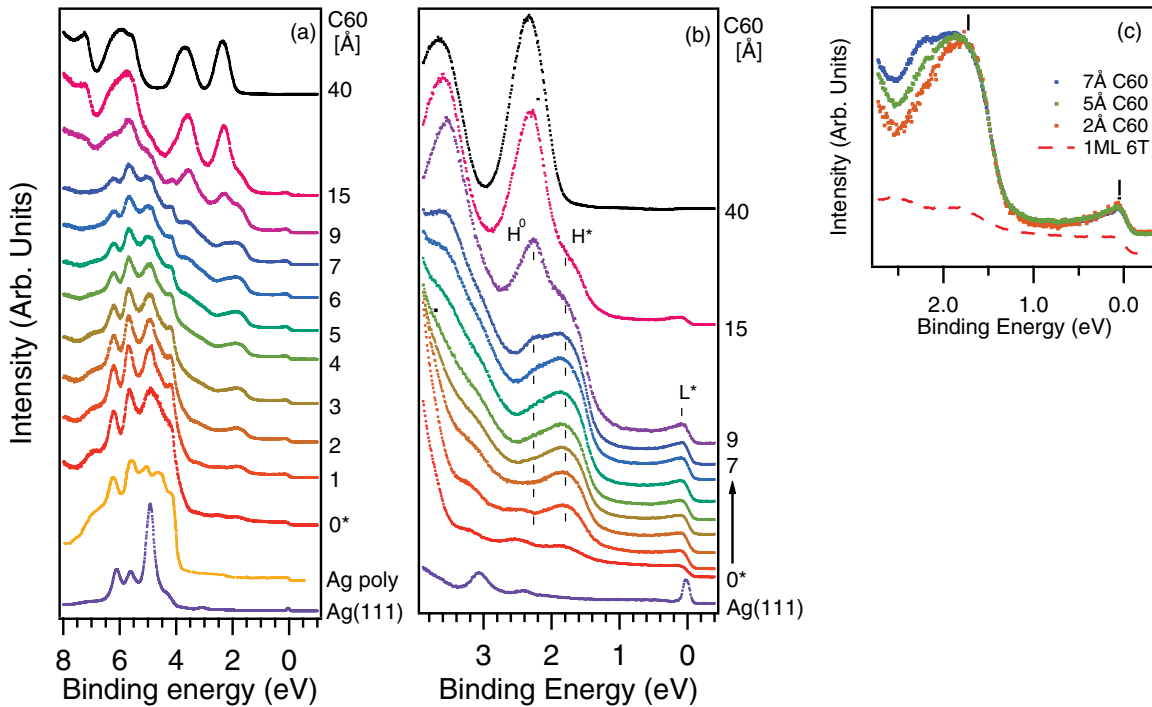


FIG. 2. (Color online) (a) From bottom to top: Valence band (VB) spectra of Ag(111), of a polycrystalline Ag sample, of ML 6T/Ag(111) and evolution of the valence band upon increasing C_{60} thickness on ML 6T/Ag(111). On the right part of the graph, 0^* stands for ML 6T/Ag(111) and the values above for the respective C_{60} film thickness. (b) Zoom into the low binding energy region of the corresponding spectra (except for polycrystalline Ag). (c) C_{60} HOMO and Fermi level region of 2-, 5-, and 7-Å C_{60} on ML 6T/Ag(111) after background removal due to ML 6T/Ag(111) represented by the bottom dashed line spectrum. HOMO, HOMO*, and LUMO* (see text) are marked with a dash.

state to the unoccupied density of states (DOS), as previously reported for similar systems.⁴⁶⁻⁴⁹ Three features in the DOS are detected for ML 6T/Ag(111), which are assigned to the highest occupied molecular orbital levels of 6T with their peak maximum at 1.8, 2.5, and 3.2 eV BE (for the HOMO, HOMO-1, and HOMO-2, respectively), and with the 6T HOMO onset at 1.3 eV BE.³⁸ As no intragap states are observed, the 6T layer can be considered as weakly interacting with the silver surface, as suggested earlier.⁵⁰

Upon C_{60} deposition, C_{60} -related DOS clearly emerges, notably in the sp band region. In the energy region of the silver d band, Ag-related DOS spectral weight remains important up to 9-Å C_{60} , which corresponds to ~ 1 ML C_{60} (also c.f. Fig. 3). The 40-Å C_{60} spectrum is representative of a thick neutral C_{60} film with its HOMO peak maximum located at 2.35 eV BE and its onset at 1.85 eV BE. The intermediate 15-Å C_{60} spectrum is a weighted sum of the first- and second-layer C_{60} contributions, showing that the DOS corresponding to the second C_{60} layer and thick C_{60} are very similar.

In the sp band region, from the first C_{60} deposition on, an increase in intensity in the immediate Fermi-level vicinity is observed. This DOS is intersected by the Fermi level, and the system can thus be considered metallic. The spectral weight of this feature keeps increasing up to 9-Å C_{60} coverage and decreases again for thicker films, demonstrating its interfacial character. The line shape and intensity of this DOS resembles closely the partially filled LUMO-derived states observed at the C_{60}/Ag interfaces. We will thus henceforth refer to this feature as LUMO* and attribute it to a charge transfer toward

the C_{60} molecules.⁵¹⁻⁵⁴ For low C_{60} coverage, the C_{60} HOMO emission is observed with a peak maximum at 1.8 eV BE and an onset at 1.3 eV BE, i.e. at about 0.55 eV BE less than for the 40-Å C_{60} film. Notably, when going from 1- to 7-Å C_{60} , the C_{60} HOMO feature becomes increasingly broadened on its high binding energy side [see Fig. 2(c)] until a clear peak emerges in the 9-Å spectrum at the energy position of the thick C_{60} film. The C_{60} HOMO broadening is therefore attributed to the development of the intrinsic (neutral) C_{60} HOMO, denoted

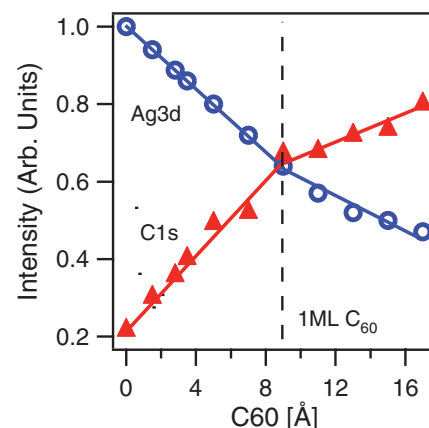


FIG. 3. (Color online) Evolution of the Ag3d (open circles) and C1s (filled triangles) relative signal intensities as a function of C_{60} thickness. The transition in the change of slopes at 9-Å C_{60} is due to the completion of the first C_{60} monolayer.

HOMO⁰ in the following. For 15-Å C₆₀, the C₆₀ HOMO⁰ peak becomes then dominant over the initially observed HOMO-related emission, whose intensity vanishes completely for the thick-film 40-Å C₆₀ spectrum. Therefore, the low BE C₆₀ HOMO is attributed to the C₆₀ interface-HOMO (i.e. the monolayer) that we denote HOMO*. Figure 2(c) shows the top VB spectra of 2-, 5-, and 7-Å C₆₀ from which the background due to ML 6T/Ag(111) has been removed, revealing the contributions due to C₆₀ only. The background removal procedure was performed consistently such that no negative intensity occurred. Nevertheless, let us remark that this procedure remains approximate because, for instance, no energy shift of the (however relatively weak) 6T features was considered, and a more detailed analysis of these spectra will be provided later on. After background removal, the spectra were normalized to the HOMO* peak maximum. This procedure highlights that the LUMO* and HOMO* intensities vary similarly for the three shown coverages. Also, the increase in intensity between 2 and 2.7 eV BE is related to the development of the intrinsic C₆₀ HOMO. The ratio of HOMO* and LUMO* spectral weight (assuming a symmetric HOMO* line shape) is ~9. Considering the fivefold degeneracy of the neutral C₆₀ HOMO and the same photoemission cross-section for both levels, the charge in the LUMO* would correspond to ~1.1 electron, which in view of the imperfect subtraction procedure, also allows for the physically reasonable value of exactly one electron in the LUMO*. Therefore, the C₆₀ HOMO*- and LUMO*-derived features are attributed to C₆₀ molecules charged with one electron, which will be referred as C₆₀⁻¹ in the following. We will see later on that the conclusions drawn from the core level spectra examination, as well as the electrostatic-based calculations, support this proposition. Note that the smaller HOMO*-LUMO* gap for C₆₀⁻¹ as compared to the HOMO-LUMO gap for C₆₀⁰ results from additional screening mechanisms due to the electron in the partially filled LUMO*.^{13,52,55}

The question of the C₆₀ growth mode is particularly important since neutral C₆₀ could be located either in the first C₆₀ layer or in subsequent layers. In a previous scanning tunneling microscopy (STM) study on the same system, no island growth mode was reported.³⁹ As STM and UPS probe film properties on different length scales, we used XPS to study the growth behavior of C₆₀ on ML 6T/Ag(111) on a macroscopic scale. The obtained normalized intensities of the C1s and Ag3d core levels (CL) signals as a function of C₆₀ nominal thickness⁵⁶ are reported in Fig. 3, which clearly shows a linear variation of both signals up to at least 9-Å thickness, beyond which the second C₆₀ layer starts to grow, as inferred from the change of slopes. This evidences that no 3D islands form before 9-Å nominal thickness, which is thus assumed to represent the complete C₆₀ monolayer. Therefore, these results allow us to conclude that the C₆₀ ML is composed of a mixture of neutral (C₆₀⁰) and anionic (C₆₀⁻¹) molecules.

In the following, XPS is used to probe the different chemical states of the molecules present at the surface and will serve as an additional tool to investigate the electrostatic potentials induced by the interfacial charge transfer.

In Fig. 4(a), the S2p CL of 6T for ML 6T/Ag(111), 3-Å (0.33 ML) C₆₀ and 7-Å (0.77 ML) C₆₀ are presented. Upon 3-Å C₆₀ deposition, the S2p shifts toward lower BE by 0.17 eV, then by an additional 0.2 eV for 7-Å C₆₀. As the S2p shift

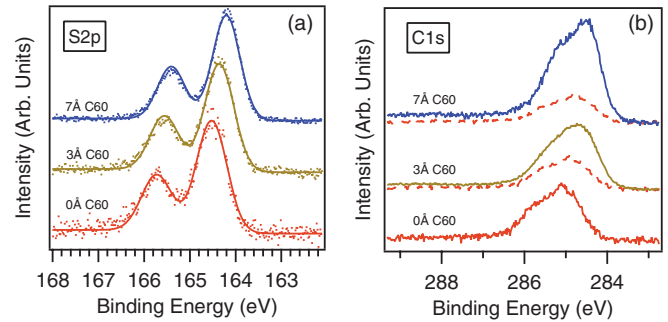


FIG. 4. (Color online) (a) Normalized S2p CL spectra of pristine ML 6T on Ag(111) (bottom) and after deposition of 3- and 7-Å C₆₀. (b) C1s CL spectra of the same systems. The spectra symbolized by dashed lines below the C1s spectra represent the 6T contribution (see text).

is gradual and without significant broadening of the peaks, it does not result from a change in the chemical state of the 6T molecules. Therefore, it is of electrostatic origin, and the shift magnitude depends on the amount of deposited C₆₀. Consequently, we relate this shift to the total amount of charges transferred from the silver to the C₆₀ overlayer. Figure 4(b) shows the corresponding C1s CL spectra. To determine the C₆₀ C1s contribution of these spectra, the as-measured spectrum is displayed together with the 6T C1s spectrum. The latter is displayed, for each coverage, shifted in energy like the S2p CL and with its intensity renormalized consistently with the Ag MNN Auger peak intensity attenuation, as shown in Ref. 38. Note that a shift of the 6T C1s spectrum has also to be considered to account for the fact that there is no shoulder due to the 6T features on the high BE tail of the C1s spectra. This is consistent with previous reports on similar systems showing that a potential drop within the spacer layer rigidly shifts all its energy levels.^{37,38}

By subtracting the 6T C1s part of the as-measured 3- and 7-Å C₆₀ spectra, the C₆₀ C1s contributions are obtained, which are presented together with the result of a fitting procedure in Figs. 5(a) and 5(b), respectively. These spectra clearly demonstrate two C₆₀ C1s contributions separated by ~0.74 eV, which can be attributed from the relative spectral weight evolution to the C₆₀⁰ and C₆₀⁻¹ at high and low BE, respectively. This interpretation compares well with what was reported by Macovez *et al.* for the surface of the face-centered cubic (fcc) phase of RbC₆₀ films where these two charge states have also been observed.⁵² Our fit results give a C₆₀⁰:C₆₀⁻¹ ratio of 1:2 and 1:1.2 for 3- and 7-Å C₆₀, respectively.

Noteworthy, these findings also imply that, if electron fluctuations occur between different C₆₀ molecules, the fluctuation timescale is much longer than the typical timescale of the photoemission process (~1 fs), as the CL spectra of the ML are not notably broadened compared to those of thick films. Also, this suggests that charge transport does not occur via band transport (delocalization) but rather via a hopping process, as expected in narrow band materials such as fullerides.⁵²

It is now possible to evaluate details of the VB spectra line shapes by simulating them via a summation including (i) two C₆₀ contributions (C₆₀⁰ and C₆₀⁻¹) whose proportions were determined from the fit results in Fig. 5; (ii) a shifted 6T contribution, with the same shift as observed for the S2p CL;

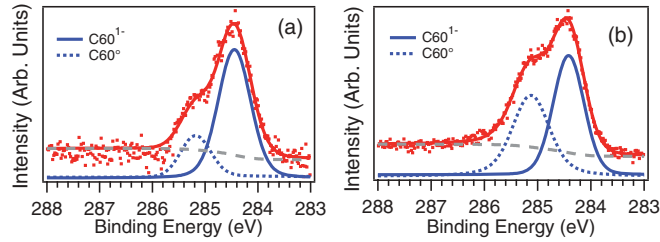


FIG. 5. (Color online) Deconvolution of the C1s C_{60} CL spectra of (a) 3-Å and (b) 7-Å C_{60} on ML 6T, obtained after subtraction of the 6T contribution from the as-measured C1s spectra presented in Fig. 4(b). The blue dots and blue lines correspond to the Gaussian components used to fit the experimental C1s spectra (red dots). The gray dotted lines represent the employed Shirley background. The red lines show the result of the fits.

and (iii) a valence band spectrum of a polycrystalline Ag (most appropriate because of the surface Umklapp experienced by the silver photoelectrons upon crossing the molecular layers). In Figs. 6(a) and 6(b), the VB spectra simulations are shown for the 3- and 7-Å C_{60} coverages and compared to the as-measured spectra. The experimental spectra are remarkably well reproduced using the $C_{60}^0:C_{60}^{-1}$ ratio determined from the C1s spectra. We want to point out that the two C_{60} VB spectra employed in the simulations are the ones of the thick film (i.e. neutral molecules) located at the energy position as observed in the 40-Å C_{60} film to represent the neutral species, and the same but shifted by 0.55 eV to lower BE without additional broadening to account for the anion contribution. The 6T DOS is simulated by the appropriately shifted spectrum of a thick, pristine film 6T/Ag(111).

2. Work function evolution

Secondary electron cutoff spectra, from which the work function (Φ) is determined, are shown in Fig. 7. Upon formation of ML 6T /Ag(111), Φ decreases from 4.55 eV [clean Ag(111)] to 3.85 eV. As 6T weakly interacts with Ag(111), this Φ decrease can be attributed to the pushback of metal electrons spilling out into vacuum from the surface.^{9,10,57,58}

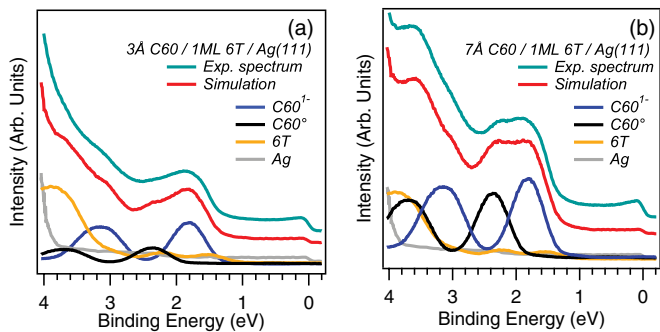


FIG. 6. (Color online) (a) and (b) at the top: As-measured VB spectra of 3- and 7-Å C_{60} /ML 6T/Ag(111), respectively, compared with simulated VB spectra (red lines) resulting from the summation of (bottom spectra) one C_{60} bulklike spectra (C_{60}^0 , black lines), a shifted C_{60} bulklike spectra (C_{60}^{-1} , blue line), a shifted 6T bulklike spectrum (orange lines), and the spectrum of a polycrystalline Ag sample (gray lines); details concerning the magnitude of the shifts and the relative C_{60} spectral weights are provided in the text).

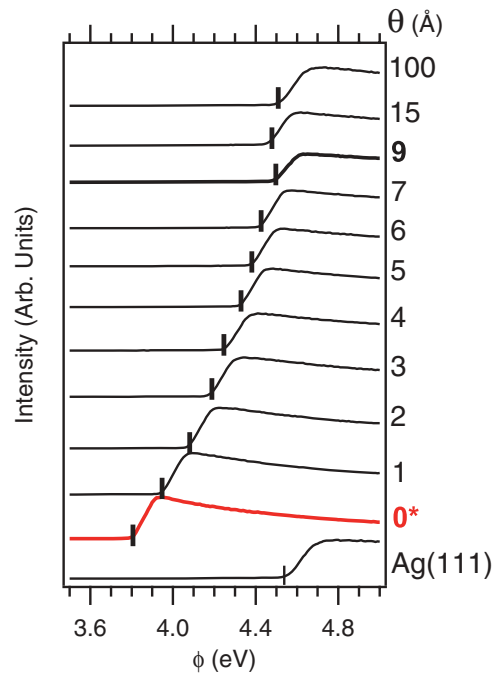


FIG. 7. (Color online) Secondary electron cutoff spectra for Ag(111), ML 6T /Ag(111) (red line, denoted 0*), and for increasing C_{60} thickness. Here, 9-Å C_{60} represent the 1-ML C_{60} /ML 6T/Ag(111) system.

Upon 15-Å C_{60} deposition, Φ increases back to 4.55 eV and remains constant for higher C_{60} coverages, demonstrating the formation of an abrupt interface dipole upon C_{60} adsorption, which in view of the previous conclusions, has to be related to the electron transfer toward a part of the C_{60} ML. The increase of Φ is not linear with coverage despite the fact that no C_{60} 3D islands form before completion of the C_{60} monolayer. Therefore, this nonlinearity in the Φ vs coverage dependence has to be related with the variation in the fraction of charged and neutral species within the C_{60} monolayer, in line with the phenomenological model developed by Topham *et al.*²⁰

This is further supported by comparing the dependence of Φ on coverage with the HOMO*, HOMO* + HOMO⁰, and LUMO* spectral weights, as depicted in Fig. 8(a). There, it can be seen that the spectral weight in the region including the HOMO⁰ and HOMO* increases linearly with C_{60} coverage, while the spectral weight of the HOMO* and LUMO* both increase asymptotically, very similar to the Φ profile. This shows unambiguously that the Φ change is determined by the absolute amount of charges transferred to the C_{60} layer and that depolarization plays no considerable additional role. The curves in Fig. 8(a) can be used to extract the fractions of C_{60}^{-1} [$\rho(\theta)$] and C_{60}^0 [$1 - \rho(\theta)$] as a function of C_{60} coverage (θ) within the monolayer range. As depicted in Fig. 8(b), $\rho(\theta)$ varies linearly with θ . Here, $\rho(\theta)$ can then be written in the form

$$\rho(\theta) = b - \alpha\theta, \quad (1)$$

where b and α are constants whose values are deduced from the graph in Fig. 8(b) and amount to ~ 0.81 and $\sim 0.42 \text{ ML}^{-1}$, respectively.

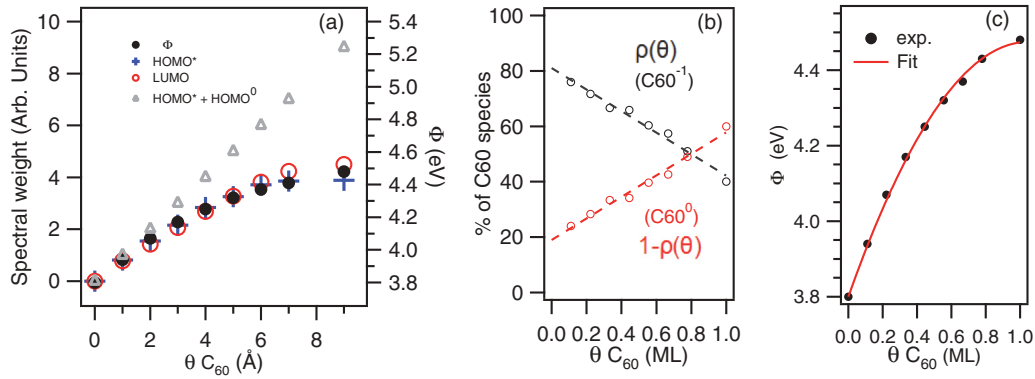


FIG. 8. (Color online) (a) Φ profile (black dots) compared to the spectral weight evolution of HOMO⁰ + HOMO* (gray triangle), HOMO* (blue cross), and LUMO* (red circles). (b) Evolution of the proportion of C₆₀⁻¹ [$\rho(\theta)$] (black open circles) and C₆₀⁰ [$1 - \rho(\theta)$] (red open circles) as a function of C₆₀ coverage within the submonolayer regime as deduced from graph (a) (see text). (c) Fit of the work function profile using [Eq. (3)] and parameter values given in the text.

The net Φ increase as a function of θ is given by the relation

$$\Delta\Phi(\theta) = \theta\rho(\theta)\Phi_0, \tag{2}$$

where Φ_0 corresponds to the work function increase for an assumed complete C₆₀ charged layer, i.e. when considering a molecular layer composed of only C₆₀⁻¹. As $\rho(\theta)$ shows a linear dependence as a function of C₆₀ coverage, inserting Eq. (1) into Eq. (2) gives

$$\Delta\Phi(\theta) = b\theta\Phi_0 - \alpha\theta^2\Phi_0. \tag{3}$$

Fitting the work function profile [Fig. 8(c)] using b and α found previously allows determining a value of 1.6 eV for Φ_0 . Interestingly, the form given by Eq. (3) is similar to the one obtained from the depolarization model by Langmuir and recently found in the case of TTF/Au(111), where it was attributed to depolarization-induced decrease in charge transfer when increasing the adsorbate density at the surface;^{59,60} however, the physical origin of our formalism is entirely different from the one in Refs. 59 and 60. We finally note that the fraction of neutral and charged C₆₀ amounts to 58% and 42%, respectively, for the complete monolayer.

B. Comparison of C₆₀ adsorbed on 1- and 2-ML 6T on Ag(111)

In this subsection, we study the dependence of the adsorption features of C₆₀ on the 6T spacer layer thickness and establish a comparison between ML 6T and BL 6T (\equiv 2-ML 6T) on Ag(111).

The SECO and VB regions of C₆₀ on top of BL 6T are shown in Fig. 9. Upon C₆₀ adsorption, the formation of an interface dipole is observed, and Φ increases from 3.8 to 4.5 eV for a thick C₆₀ film. Furthermore, the Φ profile displayed in Fig. 9(c) shows that Φ does not increase linearly with coverage but varies in a similar fashion as was observed when the 6T spacer layer film was 1 ML. The VB spectra exhibit qualitatively the same features as encountered previously, namely (i) a C₆₀ partially filled LUMO (LUMO*), and (ii) the HOMO region is composed of two contributions corresponding to HOMO⁰ and HOMO* due to C₆₀⁰ and C₆₀⁻¹. Furthermore, it can be also seen that the relative intensity of HOMO⁰ increases with respect to that of HOMO* as a function of coverage. Additional details and STM images can be found in Ref. 38.

In the following, we show how the C₆₀⁰/C₆₀⁻¹ ratio for a complete C₆₀ layer is influenced as a function of the 6T spacer

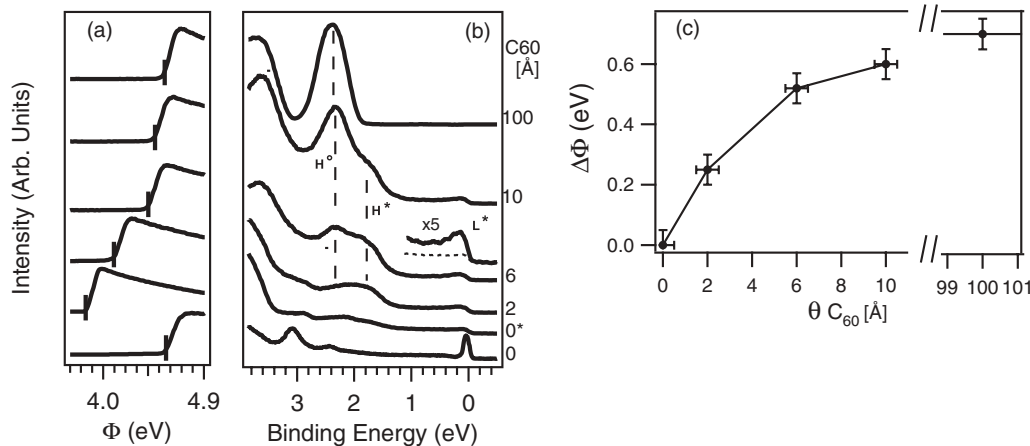


FIG. 9. SECO (a) and VB (b) spectra of C₆₀ deposited on top of a BL 6T/Ag(111). C₆₀ thicknesses are indicated on the right. 0* denotes the BL 6T film. A magnification of the E_F -region of the 6-Å C₆₀ spectrum is shown together with the adequately attenuated 6T background (dashed line). (c) Evolution of the work function as a function of C₆₀ coverage. [Part (a) and (b) reproduced from Ref. 38].

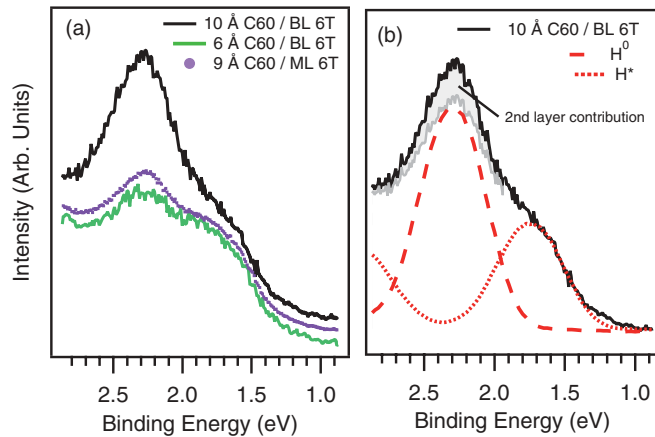


FIG. 10. (Color online) (a) Comparison of the HOMO region for 9-Å C_{60} /ML 6T (purple dotted curve), 6-Å C_{60} /BL 6T (green solid curve), and 10-Å C_{60} /1BL 6T (black curve). The spectra are normalized to the HOMO* intensity in order to reflect the relative HOMO⁰ and HOMO* intensities. (b) HOMO region of 10-Å C_{60} /BL 6T (black curve). The gray area is the estimated spectral weight due to second C_{60} layer (see text). The Gaussian curves (dotted lines) shows the relative intensities of HOMO* (0.3) and HOMO⁰ (0.7) in the first C_{60} layer.

layer thickness. Figure 10(a) shows a superimposition of the VB spectra of 6- and 10-Å C_{60} on BL 6T/Ag(111) and 9-Å C_{60} on ML 6T/Ag(111). The spectra are normalized to the HOMO* intensity in order to reflect the variation of neutral and charged species of these systems. We see that the C_{60}^0 and C_{60}^{-1} fractions for 1-ML C_{60} /ML 6T and 0.66-ML C_{60} /BL 6T are very similar.

The 10-Å C_{60} /BL 6T, which represents ~ 1.1 C_{60} ML (as determined from Fig. 3), shows a pronounced increase in C_{60}^0 intensity. The estimated spectral weight due to the second C_{60} layer, assumed to correspond only to C_{60}^0 , is depicted by the gray area and amounts to slightly less than 10% of the total spectral weight. Still, the spectral weight of C_{60}^0 within the first C_{60} layer is much larger than what was observed for 1-ML C_{60} /ML 6T. The C_{60}^{-1} and C_{60}^0 fractions for 1-ML C_{60} on BL 6T are estimated to be ~ 0.3 and ~ 0.7 , respectively, as deduced from the fitting procedure of the HOMO region shown in Fig. 10(b).

The XPS spectra also present similar features as observed when ML 6T is used as spacer layer: The C1s spectra (not shown) are composed of two components resulting from the presence of neutral and charged C_{60} molecules³⁸ and the S2p spectra, displayed in Fig. 11, exhibit a gradual shift to lower BE upon C_{60} deposition. However, the shift of the S2p spectrum is ~ 0.15 eV larger than for the ML 6T case. The fitting procedure shown in Fig. 11 helps discriminating between the first and second 6T layer contributions, which are separated by 0.4 eV in BE before C_{60} deposition. This energy difference is attributed mainly to differences in screening of the photoholes⁵ and compares well with the energy difference of 0.35 eV that was identified for the HOMO and HOMO-1 of the first and second 6T layer.³⁸ In addition, upon increasing C_{60} thickness up to 1-ML C_{60} , the full width at half maximum (FWHM) of the S2p 3/2 component decreases by 0.15 eV from 0.95 to 0.8 eV. The fitting reveals that this is due to a differential shift

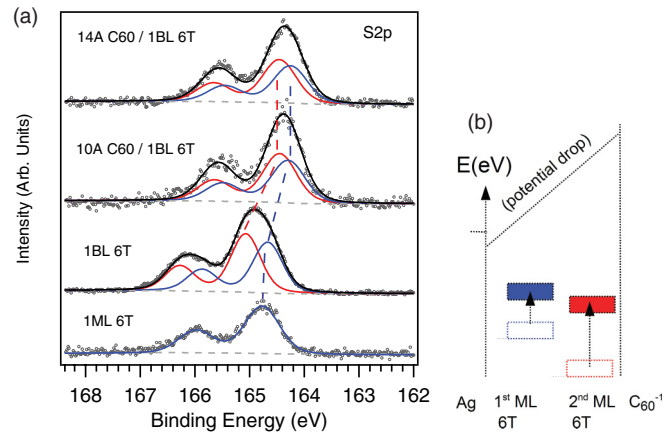


FIG. 11. (Color online) (a) S2p spectra obtained for (from bottom to top) ML 6T/Ag(111), BL 6T/Ag(111), and 10-Å and 14-Å C_{60} deposited on BL6T/Ag(111). Gray circles correspond to the experimental spectra. Blue and red lines correspond to the fit of the first and second 6T layer contributions, respectively. The black lines depict the result of the fit for each spectrum. Further details on the results of the fits are given in the text. (b) Scheme of effect of the potential drop on the relative position of the first and second layer 6T CL before (empty rectangles) and after (filled rectangles) C_{60} deposition.

of the CL corresponding to the first (0.3-eV shift) and second (0.5-eV shift) 6T layer, which leave the two contributions separated by 0.2 eV after completion of the C_{60} monolayer. Importantly, this evidences an electrostatic potential drop in the direction normal to the sample. This can be explained qualitatively by the potential drop induced by the charge transfer from the Ag(111) to a fraction of the C_{60} molecules and is further quantified in Sec. III. D below.

The similarities displayed by the two just-discussed systems strongly suggest that the mechanism governing the energy level alignment is the same in both cases. Because of the pushback effect occurring upon 6T adsorption, the metal work function is decreased by 0.7 to 3.85 eV, well below the pinning work function ($\Phi^{\text{pin-}} = 4.5$ eV) of C_{60} . The C_{60} electron affinity (EA), being ~ 4.0 eV,^{61,62} simple VL alignment between C_{60} and 6T/Ag(111) would position the C_{60} LUMO below E_F . Therefore, in order to establish electronic equilibrium, negative charge has to be transferred to C_{60} and an interface dipole is created.

Whenever considering a molecular heterojunction where E_F pinning occurs, the charge transfer is often associated to occur right at the interface between the two molecular layers. However, in most cases the ionization energy (IE) and EA of the materials employed have a large energy mismatch (as in the present case where the difference of the 6T IE and the C_{60} EA amounts to ~ 1 eV) such that, based on general grounds, no intermolecular charge transfer is expected.

In the case of the C_{60} /6T interface, a charge transfer between the molecules can be ruled out as it is not observed when the substrate employed has a higher work function and the 6T layer has a similar thickness.⁶³ In fact, none of the features shown above (including the interface dipole formation, the 6T core levels shifts, and the two distinct C_{60} C1s components) were reported in Ref. 63. Also, for the present systems, considering an intermolecular charge transfer would not

explain the fact that different charge states are observed within the C_{60} layer and not within the 6T layer. Furthermore, invoking intermolecular charge transfer does not provide a satisfactory explanation for the fact that the fraction of the two C_{60} species depends on the 6T spacer layer thickness. This allows concluding that the effect of intermolecular interactions (involving charge transfer or hybridization) is very small and plays a negligible role in explaining our observations.

Rarely discussed is the possibility that charges in the overlayer (responsible for interface dipoles) come from the substrate as proposed in the MOCT model. However, this is a very reasonable assumption, as the molecular level alignment is actually determined by the electron chemical potential of the substrate, as already clearly phrased by the term ‘‘Fermi-level pinning’’, which acts as an electron reservoir for establishing electronic equilibrium. In the following, we closely examine this proposition, and we show that under this consideration it is possible to draw a coherent picture that allows explaining the experimental observations quantitatively. Electrostatic considerations are employed to address the questions why (i) the C_{60} layer is not homogeneously charged; (ii) the fraction of charged and neutral molecules varies with the 6T spacer layer thickness; and (iii) C_{60} molecules, which do not undergo charge transfer in the monolayer, can still be at electronic equilibrium within that layer. To do so, we first treat the impact of dipole-dipole interactions on these systems qualitatively and then quantify the electrostatic potential change induced in the vicinity of charged C_{60} molecules.

C. Effect of dipole-dipole interactions

For MOCT through a spacer layer as proposed in this paper, one has to deal with large dipole moments, oriented normal to the sample surface and formed by charges in the overlayer and their counterparts inside the metal. Thus, the impact of dipole-dipole interactions cannot be neglected anymore.^{21,38,60,64} For such systems, the minimization of the total energy will result from the energy gain due to the charge transfer (corresponding to the energy difference between E_F and the LUMO), which is balanced by the electrostatic potential created by the charges in the molecular layer. This potential, which can extend up to a few nanometers,^{64,65} can be modeled classically in the framework of the image charge model. To do so, one has to consider the (repulsive) electron-electron and (attractive) electron-image charge interactions, as depicted in Fig. 12. In this case, the interaction potentials can be approximated in a classical way by the relation

$$U(d) = \frac{q}{4\pi\epsilon_r\epsilon_0} - \frac{2q^2}{4\pi\epsilon_r\epsilon_0\sqrt{(2z)^2 + d^2}}$$

$$= \frac{q^2}{4\pi\epsilon_r\epsilon_0 d} \left(1 - \frac{2}{\sqrt{1 + \left(\frac{2z}{d}\right)^2}} \right), \quad (4)$$

where d is the horizontal distance between the two dipoles, and z is the distance between an electron (described a point charge) and the image plane. Note that, in this model, as we aim to investigate the role of lateral interactions, the attractive interaction between each electron and its image, which would add an offset to $U(d)$, is neglected. In Fig. 12,

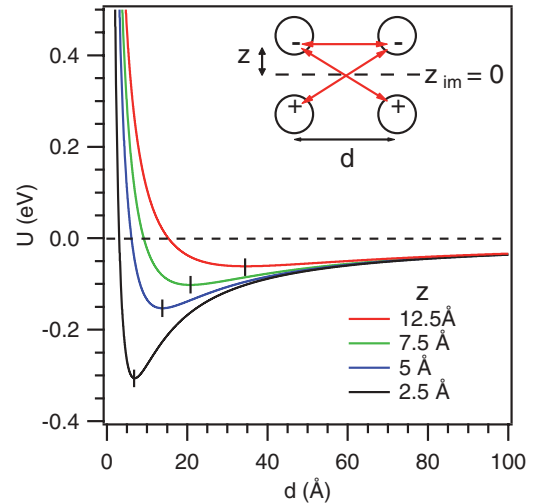


FIG. 12. (Color online) Interaction potentials between two dipoles formed by electrons and their image charge in the metal as a function of d , the distance between two adjacent dipoles, and for different electron-image charge distances $2z$, ranging from 5 to 25 Å (from bottom to top). The vertical lines show the position of minimum energy for each profile. Inset: Geometry of the considered system; the red arrows show the interactions taken into account in the model. Here, Z_{im} is the position of the image plane.

typical interaction potential profiles obtained from Eq. (4) with $\epsilon_r = 4$ (Refs. 66–68) are shown as a function of d and for different fixed z . The profiles depicted with $z = 5$ and 7.5 Å are representative of the C_{60}/ML 6T/Ag(111) and C_{60}/BL 6T/Ag(111) cases, respectively, similarly to the metal–charge distances used in the Helmholtz equation in the next section. Note that these distances imply that the electron is located at the bottom part of the C_{60} molecules, which can be intuitively justified by considering the attraction between the charge and its image. Of course, describing the electrons as point charges remains an approximation to the actual spatial extent of the frontier π orbitals, which are delocalized and also tail out of the C_{60} cage.

The profiles in Fig. 12 show that the interdipole potential is repulsive in the low d limit, then turns to be attractive when d increases and exhibits a minimum for $d = 2.6z$. Noticeably, one clear energy minimum emerges in each profile, at ~ 13 and ~ 19.6 Å for $z = 5$ and 7.5 Å, respectively. From a qualitative point of view, since the equilibrium distance between two dipoles (= distance between two charges in the overlayer) increases as a function of z , this allows rationalizing why the C_{60}^{-1}/C_{60}^0 ratio decreases when increasing the 6T spacer layer thickness (see Fig. 9). Note that these equilibrium distances are consistent with the surface density of C_{60}^{-1} determined experimentally for 1-ML C_{60}/ML 6T/Ag(111) (0.45 nm^{-2}) and 1-ML C_{60}/BL 6T/Ag(111) (0.3 nm^{-2}) when considering a compact C_{60} monolayer. We further remark that numerous similarities are found between the present experimental findings (Φ profile and varying proportion of charged and neutral molecules) and the predictions of the charge transfer model developed by Topham *et al.* where dipole-dipole repulsion is a key point.²⁰ In a more general picture, it is also interesting to notice that the gain in energy

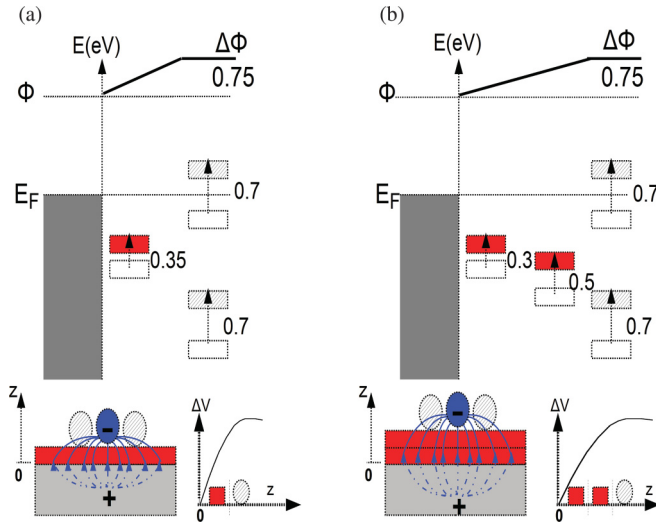


FIG. 13. (Color online) Energy level diagram for (a) 1-ML C_{60} /ML 6T/Ag(111) and (b) 1-ML C_{60} /BL 6T/Ag(111). Empty rectangles depict the energy position of 6T HOMO, neutral C_{60} HOMO, and neutral C_{60} LUMO assuming VL alignment (before contact). Filled rectangles show the actual energy level alignment as determined experimentally. The difference between both, depicted by the arrows and the associated numbers, results from the potential drop due to the dipoles formed with charged C_{60} molecules. At the bottom part of the figure, the electric field lines and the potential drop ΔV as a function of z are depicted for each system.

due charge transfer, defined as the energy difference between E_F and the energy position of the partially filled molecular orbital will be balanced by the electrostatic potential described above, so that the total energy of the system is minimized. For a comprehensive understanding of the energy level alignment, one has to further consider the potential drop in between two charges (in vertical direction). In the following, we therefore address the impact of the electric field produced by these dipoles, which plays a major role in allowing the neutral C_{60} molecules in the overlayer to be at electronic equilibrium without undergoing a charge transfer.

D. Energy level alignment and electrostatic considerations

It has been reported that C_{60} $\Phi^{\text{pin-}}$ is 4.5 eV,^{23,25} which means that for a sample having a Φ smaller than 4.5 eV, charge transfer must occur to establish electronic equilibrium (i.e. to prevent that the empty C_{60} LUMO is located below E_F). As the work function of 6T/Ag(111) is 3.8 eV, the neutral C_{60} HOMO peak maximum should be found at 3 eV BE (and its onset at

2.5 eV BE) when assuming VL alignment. Given a charge transport gap (determined from HOMO and LUMO onset energy difference) of about 2.4 eV as determined by combined direct and inverse photoemission,^{61,62} electronic equilibrium would not be encountered for these molecules. In contrast, the present results show that the HOMO peak maximum of the neutral C_{60} is positioned at 2.3 eV BE (and onset at ~ 1.8 eV), i.e. where the neutral C_{60} molecules are electronically stable. We will now demonstrate that the discrepancy between the expected neutral C_{60} HOMO BE assuming VL alignment and the actual one is due to the potential drop, which was also found to affect the 6T CL. The magnitude of the potential drop and its influence on the energy level diagram, as deduced from experiments, are resumed in Fig. 13. The energy position of the neutral C_{60} HOMO is now reconsidered by accounting for electrostatic fields arising from MOCT. It is possible to calculate the change in the electrostatic potential induced upon C_{60}^{-1} adsorption within the image charge model in order to test the previous assumptions. For this, we consider an ordered network of dipoles (corresponding to anion C_{60} molecules) and their mirror charge in the metal substrate, which are described as negative and positive point charges, respectively.

The 1-ML C_{60} /ML 6T/Ag(111) and 1-ML C_{60} /BL 6T/Ag(111) systems are simulated as a square network of C_{60}^{1-} whose dimensions give an C_{60}^{1-} areal density (N) in agreement with the experimentally observed C_{60} fractions. The electron-image plane distance z is chosen such that the electron in the charged C_{60} is located at the bottom part of the molecule (see Table I), as mentioned earlier. The employed values are listed in Table I together with the ones determined experimentally.

The expected work function increase can be calculated by the Helmholtz equation⁶⁹

$$\Delta\Phi = (qNp)/(\epsilon_0\epsilon_r), \quad (5)$$

with q the elementary charge, p the dipole moment perpendicular to the surface, N the areal density of C_{60}^{-1} , ϵ_0 the vacuum permittivity, and ϵ_r the relative dielectric constant. With a charge transfer of one electron and $\epsilon_r = 4$,⁶⁴⁻⁶⁶ we find $\Delta\Phi = 0.85$ eV for 1-ML C_{60} /ML 6T and $\Delta\Phi = 0.87$ eV for 1-ML C_{60} /BL 6T.

The potential drop ΔV within the molecular layers at a point M can be seen as the sum of the potentials created by the positive and negative monopoles on each side of the image plane and can be expressed by

$$\Delta V(M) = \frac{1}{4\pi\epsilon_r\epsilon_0} \sum_i \frac{q_i}{r_i(M)}, \quad (6)$$

TABLE I. Experimental and theoretical values employed in Eqs. (5) and (6) to determine the theoretical $\Delta\Phi$ and potential drop. Details on the potential drop profile are provided in Fig. 14.

	C_{60}^{-1} fraction (experimental)	C_{60}^{-1} (N , theoretical)	z (\AA , theoretical)	$\Delta\Phi$ [eV, E(5)]		Potential drop (eV, experimental)			Potential drop [eV, E(6)]		
				Experimental	Theoretical	First 6T	Second 6T	C_{60}	First 6T	Second 6T	C_{60}
1-ML C_{60} / ML 6T	0.42	0.42	4.5	0.75	0.85	0.35	0.7	0.3	0.65		
1-ML C_{60} / BL 6T	0.3	0.28	7	0.75	0.87	0.3	0.5	0.7	0.25	0.45	0.65

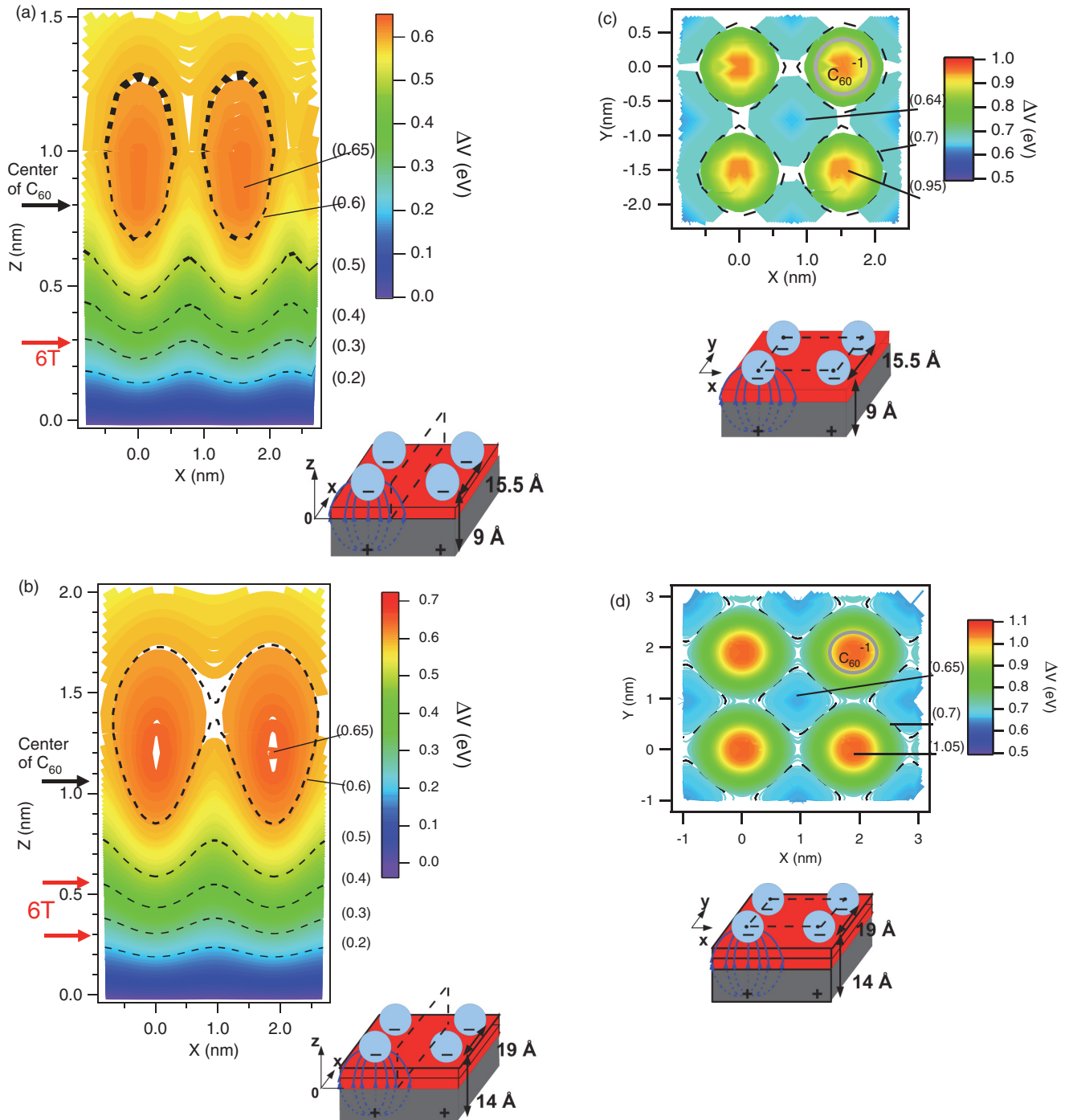


FIG. 14. (Color online) Map of the potential increase ΔV for (a) C60/ML 6T/Ag(111) and (b) C60/BL 6T/Ag(111) within the plane normal to the surface as schematically depicted in inset. The arrows on the left represent the approximate position of the 6T layers. (c) and (d) Map of the potential increase (ΔV) for C60/ML 6T/Ag(111) and C60/BL 6T/Ag(111), respectively, within the plane parallel to the surface 2 Å above the location of the point charges (i.e. going through the center of the C₆₀ molecules). Note that the point charges are located below the higher ΔV values in the graph. The dotted lines on the potential map present the isocontours corresponding to the values in between parenthesis.

where q_i corresponds to the charge of the i th monopole and $r_i(M)$ represents the distance between the i th monopole and any point M in the space. A map of the resulting increase in potential ΔV in a plane normal to the sample is shown in Figs. 14(a) and 14(b) for C₆₀ on ML 6T and BL 6T, respectively.

From these calculations, the potential at the adsorption sites of neutral C₆₀ is seen to increase by $\sim 0.6\text{--}0.65$ eV for 1-ML C₆₀/ML 6T and $\sim 0.6\text{--}0.7$ eV for 1-ML C₆₀/BL 6T, consistent with the expectation of 0.7 eV, as mentioned earlier. Furthermore, the potential increase within the 6T layer is in very good agreement with the experimental data and even

reproduces the differential shift of the 6T features observed in the XPS spectra of BL 6T (see Fig. 11). The averaged numerical results are resumed in Table I.

Maps of the induced electrostatic potential in a plane parallel to the surface and cutting through the center of the C_{60} molecules are displayed in Figs. 14(c) and 14(d). The potential is rather homogeneous in the xy plane and therefore not expected to lead to a significant broadening of the neutral C_{60} HOMO, again consistent with the experimental observations. Note that test calculations including charges homogeneously spread over small disks (with diameter of 0.8 nm corresponding to the diameter of a C_{60} molecule) instead of point charges were also performed and gave comparable results.

Finally, we comment on the consequences of the present findings on the energy level alignment at molecular (organic) heterojunctions in contact with a metal, or, more generally, conductive electrodes and presenting similar energy level structures. For these systems, even though in most cases interface dipoles are observed, photoemission measurements do not reveal DOS at E_F that could be directly attributed to charge transfer to the organic overlayer. The analysis provided in this study might help in understanding this discrepancy. Indeed, the fact that not all molecules are charged may allow attributing the lacking of DOS at the Fermi level for those other cases as being due to a much too small amount of charges at the interface to be detected. In a first approximation, the density of dipoles resulting from electrode-to-overlayer charge transfer necessary to create the observed work function changes is expected to vary inversely proportional with the overlayer—electrode distance. As a result, the density of dipoles will be dramatically reduced when increasing the organic spacer layer thickness.

To test our assumption, we have applied the electrostatic calculations presented above to the recently reported system diindenoperylene (DIP) grown on 10-nm C_{60} adsorbed on a conductive polymer electrode made of poly(ethylenedioxythiophene:polystyrenesulfonate (PEDT:PSS)²⁹ with an initial $\Phi = 5.55$ eV for C_{60} /PEDT:PSS. In this study, E_F pinning was found for the DIP HOMO, and Φ decreased by 0.45 eV as a result of the creation of an interface dipole by adsorption of the first DIP layer. The DIP HOMO onset was measured at 0.3 eV BE, and no DOS was observed at E_F . Because DIP has an IE of 5.4 eV, VL alignment would have placed its HOMO onset 0.15 eV above E_F . Furthermore, upon DIP deposition, the HOMO of the C_{60} spacer layer continuously shifted to higher BE by 0.25 eV. Figure 15(a) resumes the actual energy level diagram of this system and the expected one in the hypothetical case of VL alignment. Considering the negative end of the interface dipole located at the substrate surface and the positive one in the first DIP layer, and applying the Helmholtz equation to this system, it is found that a dipole density of 0.01 nm^2 (i.e. one charged DIP molecule for $\sim 100 \text{ nm}^2$) is sufficient to induce the observed work function decrease. The potential drop as determined with Eq. (6) shows a homogeneous potential decrease of $\sim 0.27 (\pm 0.03)$ eV in the topmost C_{60} spacer layer and in the DIP overlayer as shown in Fig. 15(b). Therefore, these values are consistent with the experimental observations and help in explaining the lack of easily observable charged DIP

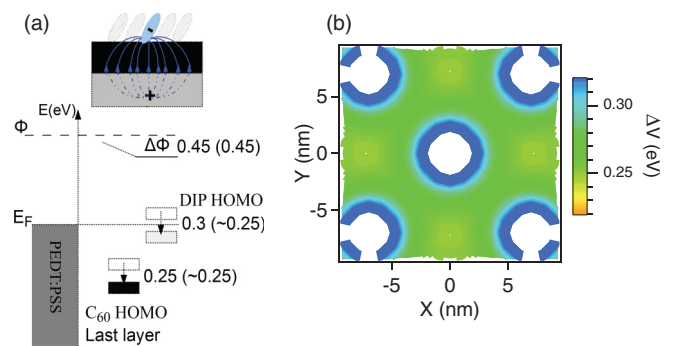


FIG. 15. (Color online) (a) Energy level diagram of DIP/10 nm C_{60} /PEDT:PSS from Ref. 29. Filled rectangles show the actual energy level alignment and empty rectangle the energy level alignment when assuming VL alignment. The difference between both, depicted by the arrows and the associated numbers, results from the potential drop due to the dipoles formed with charged DIP molecules in the overlayer. Values between parentheses are the average energy shift determined theoretically. (b) Shows the potential map in the last C_{60} layer as calculated with Eq. (6) (see text). The isocontours are plotted for a potential drop comprised between 0.22 eV and 0.32 eV.

molecules. Therefore, this suggests that the model developed in this paper may be valid (within the model's limitations) to adequately explain the electronic properties of many application-relevant organic-organic interfaces.

IV. CONCLUSIONS

We have incrementally deposited C_{60} on substrates consisting of ML 6T and BL 6T on Ag(111) and followed the evolution of Φ and VB during interface formation. For 6T covered Ag(111), Φ is well below $\Phi^{\text{pin-}}$ of C_{60} , and therefore upon C_{60} adsorption an interface dipole arises. Remarkably, the work function is found to increase asymptotically. The Φ increase, which is correlated with the emergence of the partially filled C_{60} LUMO in the VB spectra, results from an integer charge transfer from the metal to the C_{60} overlayer (MOCT) through the neutral 6T spacer layer. A careful analysis of the core levels and valence band (VB) spectral weights of the different contributions leads us to further conclude that two C_{60} species, namely neutral (C_{60}^0) and charged (C_{60}^{-1}), are observed simultaneously and in different proportions at different C_{60} coverages within the submonolayer regime. This varying fraction is identified as the cause for the nonlinearity of the Φ profile. When C_{60} is deposited on BL 6T on Ag(111), similar features are found with the difference that the fraction of charged C_{60} molecules is systematically lower. Dipole-dipole interaction is proposed as the driving force leading to the occurrence of a layer composed of mixed neutral and charged C_{60} species. Electrostatic considerations allow for a quantitative analysis of the energy shift of the 6T spectral features as being due to the potential drop over this neutral spacer layer. The energy level alignment at these interfaces could thus be explained in a coherent picture of integer charge transfer and associated charge dilution in the C_{60} overlayer.

Our model was applied successfully to apprehend the energy level alignment recently reported for another organic/organic interface grown on a conductive polymer

substrate. We therefore suggest that substrate-to-organic overlayer charge transfer and the resulting electric field are key prerequisites for understanding the energy level alignment at molecular and organic heterojunctions in contact with metals or conductive electrodes.

ACKNOWLEDGMENTS

We thank Martin Oehzelt and Haibo Wang for stimulating discussions. This work was supported by the SFB951 and SPP1355 (DFG), and the Helmholtz-Energieallianz “Hybrid-photovoltaik”.

*amsalem@physik.hu-berlin.de

- ¹M. A. Baldo and S. R. Forrest, *Phys. Rev. B* **64**, 085201 (2001).
- ²G. Horowitz, R. Hajlaoui, H. Bouchriha, R. Bourguiga, and M. Hajlaoui, *Adv. Mater. (Weinheim, Ger.)* **10**, 923 (1998).
- ³W. Zhao, E. Salomon, Q. Zhang, S. Barlow, S. R. Marder, and Antoine Kahn, *Phys. Rev. B* **77**, 165336 (2008).
- ⁴J. Wagner, M. Gruber, A. Hinderhofer, A. Wilke, B. Bröker, J. Frisch, P. Amsalem, A. Vollmer, A. Opitz, N. Koch, F. Schreiber, and W. Brütting, *Adv. Funct. Mater.* **20**, 4295 (2010).
- ⁵H. Ishii, K. Sugiyama, E. Ito, and K. Seki, *Adv. Mat.* **11**, 605 (1999).
- ⁶X. Zhou, M. Pfeiffer, J. Blochwitz, A. Werner, A. Nollau, T. Fritz, and K. Leo, *Appl. Phys. Lett.* **78**, 410 (2001).
- ⁷A. Kahn, N. Koch, and W. Gao, *J. Polym. Sci. B* **41**, 2529 (2003).
- ⁸I. G. Hill, A. Rajagopal, A. Kahn, and Y. Hu, *Appl. Phys. Lett.* **73**, 662 (1998).
- ⁹P. S. Bagus, V. Staemmler, and C. Wöll, *Phys. Rev. Lett.* **89**, 096104 (2002).
- ¹⁰G. Witte, S. Lukas, P. S. Bagus, and C. Wöll, *Appl. Phys. Lett.* **87**, 263502 (2005).
- ¹¹L. Romaner, G. Heimel, J. L. Brédas, A. Gerlach, F. Schreiber, R. L. Johnson, J. Zegenhagen, S. Duhm, N. Koch, and E. Zojer, *Phys. Rev. Lett.* **99**, 256801 (2007).
- ¹²R. Korytar and N. Lorente, *J. Phys.: Condens. Matter* **23**, 355009 (2011).
- ¹³J. D. Sau, J. B. Neaton, H. J. Choi, S. G. Louie, and M. L. Cohen, *Phys. Rev. Lett.* **101**, 026804 (2008).
- ¹⁴M. Dion, H. Rydberg, E. Schröder, D. C. Langreth, and B. I. Lundqvist, *Phys. Rev. Lett.* **92**, 246401 (2004).
- ¹⁵I. Hamada and M. Tsukada, *Phys. Rev. B* **83**, 245437 (2011).
- ¹⁶S. Yanagisawa, K. Lee, and Y. Morikawa, *J. Phys. Chem. C* **128**, 244704 (2008).
- ¹⁷N. Dori, M. Menon, L. Kilian, M. Sokolowski, L. Kronik, and E. Umbach, *Phys. Rev. B* **73**, 195208 (2006).
- ¹⁸N. Marom, X. Ren, J. E. Moussa, J. R. Chelikowsky, and L. Kronik, *Phys. Rev. B* **84**, 195143 (2011).
- ¹⁹A. Biller, I. Tamblyn, J. B. Neaton, and L. Kronik, *J. Chem. Phys.* **135**, 164706 (2011).
- ²⁰B. J. Topham, M. Kumar, and Z. G. Soos, *Adv. Funct. Mater.* **21**, 1931 (2011).
- ²¹G. Tomba, M. Stengel, W. D. Schneider, A. Baldereschi, and A. De Vita, *ACS Nano* **4**, 7545 (2010).
- ²²H. Vázquez, R. Oszwaldowski, P. Pou, J. Ortega, R. Pérez, F. Flores, and A. Kahn, *Europhys. Lett.* **65**, 802 (2004).
- ²³S. Braun, W. R. Salaneck, and M. Fahlmann, *Adv. Mater.* **346**, 1450 (2009).
- ²⁴W. Osikowicz, M. P. de Jong, and W. R. Salaneck, *Adv. Mater.* **19**, 4213 (2007).
- ²⁵M. Bokdam, D. Çakır, and G. Brocks, *App. Phys. Lett.* **98**, 113303 (2011).
- ²⁶M. T. Greiner, M. G. Helander, W. M. Tang, Z. B. Wang, J. Qiu, and Z. H. Lu, *Nat. Mater.* **11**, 76 (2011).
- ²⁷N. Koch, *Chem. Phys. Chem.* **8**, 1438 (2007).
- ²⁸N. Koch, S. Duhm, J. P. Rabe, A. Vollmer, and R. L. Johnson, *Phys. Rev. Lett.* **95**, 237601 (2005).
- ²⁹A. Wilke, P. Amsalem, J. Frisch, B. Bröker, A. Vollme, and N. Koch, *Appl. Phys. Lett.* **98**, 123304 (2011).
- ³⁰T. Sueyoshi, H. Fukagawa, M. Ono, S. Kera, and N. Ueno, *Appl. Phys. Lett.* **95**, 183303 (2009).
- ³¹F. Rissner, G. M. Rangger, O. T. Hofmann, A. M. Track, G. Heimel, and E. Zojer, *ACS Nano* **3**, 3513 (2009).
- ³²L. Ley, Y. Smets, C. I. Pakes, and J. Ristein, *Adv. Funct. Mater.* (2012), doi:10.1002/adfm.201201412.
- ³³A. Wilke, T. Mizokuro, R. P. Blum, J. P. Rabe, and N. Koch, *IEEE J. Sel. Top. Quantum Electron.* **16**, 732 (2010).
- ³⁴J. Frisch, A. Vollmer, J. P. Rabe, and N. Koch, *Org. Electron.* **12**, 916 (2011).
- ³⁵H. Peisert, A. Petr, L. Dunsch, T. Chassé, and M. Knupfer, *Chem. Phys. Chem.* **8**, 386 (2007).
- ³⁶J. Hwang, A. Wan, and A. Kahn, *Mater. Sci. Eng., R* **64**, 1 (2009).
- ³⁷P. Amsalem, J. Niederhausen, J. Frisch, A. Wilke, B. Bröker, A. Vollmer, R. Rieger, K. Müllen, J. P. Rabe, and Norbert Koch, *J. Phys. Chem. C* **115**, 17503 (2011).
- ³⁸J. Niederhausen, P. Amsalem, A. Wilke, R. Schlesinger, S. Winkler, A. Vollmer, J. P. Rabe, and N. Koch, *Phys. Rev. B* **86**, 081411(R) (2012).
- ³⁹H. L. Zhang, W. Chen, L. Chen, H. Huang, X. S. Wang, J. Yuhara, and A. T. S. Wee, *Small* **3**, 2015 (2007).
- ⁴⁰L. Chen, W. Chen, H. Huang, H. L. Zhang, J. Yuhara, and A. T. S. Wee, *Adv. Mater.* **20**, 484 (2008).
- ⁴¹J. Anderson and G. J. Lapeyre, *Phys. Rev. Lett.* **36**, 376 (1976).
- ⁴²S. A. Lindgren and L. Wallden, *Phys. Rev. Lett.* **43**, 460 (1979).
- ⁴³L. Giovanelli, P. Amsalem, T. Angot, L. Petaccia, S. Gorovikov, L. Porte, A. Goldoni, and J. M. Themlin, *Phys. Rev. B* **82**, 125431 (2010).
- ⁴⁴F. C. Bocquet, L. Giovanelli, P. Amsalem, L. Petaccia, D. Topwal, S. Gorovikov, M. Abel, N. Koch, L. Porte, A. Goldoni, and J.-M. Themlin, *Phys. Rev. B* **84**, 241407(R) (2011).
- ⁴⁵L. Giovanelli, F. C. Bocquet, P. Amsalem, H.-L. Lee, M. Abel, S. Clair, M. Koudia, T. Faury, L. Petaccia, D. Topwal, E. Salomon, T. Angot, A. A. Cafolla, N. Koch, L. Porte, A. Goldoni, and J.-M. Themlin, *Phys. Rev. B* **87**, 035413 (2013).
- ⁴⁶R. Temirov, S. Soubatch, A. Luican, and F. S. Tautz, *Nature* **444**, 350 (2006).
- ⁴⁷C. H. Schwalb, S. Sachs, M. Marks, A. Schöll, F. Reinert, E. Umbach, and U. Höfer, *Phys. Rev. Lett.* **101**, 146801 (2008).
- ⁴⁸N. L. Zaitsev, I. A. Nechaev, and E. V. Chulkov, *J. Exp. Theor. Phys.* **110**, 114 (2010).
- ⁴⁹M. S. Dyer and M. Persson, *New J. Phys.* **12**, 063014 (2010).
- ⁵⁰N. Koch, G. Heimel, J. Wu, E. Zojer, R. L. Johnson, J. L. Brédas, K. Müllen, and J. P. Rabe, *Chem. Phys. Lett.* **413**, 390 (2005).

- ⁵¹P. J. Benning, F. Stepniak, D. M. Poirier, J. L. Martins, J. H. Weaver, L. P. F. Chibante, and R. E. Smalley, *Phys. Rev. B* **47**, 13843 (1993).
- ⁵²R. Macovez, A. Goldoni, L. Petaccia, I. Marenne, P. A. Brühwiler, and P. Rudolf, *Phys. Rev. Lett.* **101**, 236403 (2008).
- ⁵³B. W. Hoogenboom, R. Hesper, L. H. Tjeng, and G. A. Sawatzky, *Phys. Rev. B* **57**, 11939 (1998).
- ⁵⁴J. Schiessling, L. Kjeldgaard, T. Kaambre, I. Marenne, J. N. O'Shea, J. Schnadt, C. J. Glover, M. Nagasono, D. Nordlund, M. G. Garnier, L. Qian, J. E. Rubensson, P. Rudolf, N. Martensson, J. Nordgren, and P. A. Brühwiler, *Phys. Rev. B* **71**, 165420 (2005).
- ⁵⁵Xinghua Lu, M. Grobis, K. H. Khoo, Steven G. Louie, and M. F. Crommie, *Phys. Rev. B* **70**, 115418 (2004).
- ⁵⁶The 6T C1s spectral weight was subtracted from the total C1s intensity in order to obtain only the intensity from the C₆₀ C1s core level. The 6T C1s signal was approximated to decrease like the Ag3d signal.
- ⁵⁷S. Duhm, Q. Xin, N. Koch, N. Ueno, and S. Kera, *Org. Electron.* **12**, 903 (2011).
- ⁵⁸S. Duhm, G. Heimel, I. Salzmann, H. Glowatzki, R. L. Johnson, A. Vollmer, J. P. Rabe, and N. Koch, *Nat. Mat.* **7**, 326 (2008).
- ⁵⁹I. Langmuir, *J. Am. Chem. Soc.* **54**, 2798 (1932).
- ⁶⁰J. Fraxedas, S. García-Gil, S. Monturet, N. Lorente, I. Fernandez-Torrente, K. J. Franke, J. I. Pascual, A. Vollmer, R. P. Blum, N. Koch, and P. Ordejon, *J. Phys. Chem. C* **115**, 18640 (2011).
- ⁶¹J. H. Weaver, *J. Phys. Chem. Sol.* **53**, 1433 (1992).
- ⁶²A. Wilke, J. Endres, J. Niederhausen, R. Schlesinger, J. Frisch, P. Amsalem, U. Hörmann, J. Wagner, M. Gruber, A. Opitz, A. Vollmer, W. Brütting, A. Kahn, and N. Koch, *App. Phys. Lett.* **101**, 233301 (2012).
- ⁶³R. Wang, H. Y. Mao, H. Huang, D. C. Qi, and W. Chen, *J. Appl. Phys.* **109**, 084307 (2011).
- ⁶⁴T. Yokoyama, T. Takahashi, K. Shinozaki, and M. Okamoto, *Phys. Rev. Lett.* **98**, 206102 (2007).
- ⁶⁵N. V. Petrova and I. N. Yakovkin, *Surf. Sci.* **519**, 90 (2002).
- ⁶⁶R. R. Zope, T. Baruah, M. R. Pederson, and B. I. Dunlap, *Phys. Rev. B* **77**, 115452 (2008).
- ⁶⁷A. F. Hebard, R. C. Haddon, R. M. Fleming, and A. R. Kortan, *Appl. Phys. Lett.* **59**, 2109 (1991).
- ⁶⁸To simplify the calculation, we used a common relative permittivity for both materials.
- ⁶⁹G. A. Somorjai, *Introduction to Surface Chemistry and Catalysis* (Wiley, New York, 1994) p. 388.